Reversible writing of high-mobility and high-carrier-density doping patterns in two-dimensional van der Waals heterostructures

Wu Shi 1,2,3, Salman Kahn 1,2,3, Lili Jiang 1,2,3, Sheng-Yu Wang 1, Hsin-Zon Tsai 1,2,3, Dillon Wong 1,2,3, Takashi Taniguchi 4, Kenji Watanabe 4, Feng Wang 1,2,3, Michael F. Crommie 1,2,3 and Alex Zettl 1,2,3*

A key feature of two-dimensional materials is that the sign and concentration of their carriers can be externally controlled with techniques such as electrostatic gating. However, conventional electrostatic gating has limitations, including a maximum carrier density set by the dielectric breakdown, and ionic liquid gating and direct chemical doping also suffer from drawbacks. Here, we show that an electron-beam-induced doping technique can be used to reversibly write high-resolution doping patterns in hexagonal boron nitride-encapsulated graphene and molybdenum disulfide (MoS₂) van der Waals heterostructures. The doped MoS₂ device exhibits an order of magnitude decrease of subthreshold swing compared with the device before doping, whereas the doped graphene devices demonstrate a previously inaccessible regime of high carrier concentration and high mobility, even at room temperature. We also show that the approach can be used to write high-quality p-n junctions and nanoscale doping patterns, illustrating that the technique can create nanoscale circuitry in van der Waals heterostructures.

xternally controlled modulation of charge density is at the heart of the semiconductor electronics industry¹. Modulation via traditional electrostatic gating has been shown to be effective for two-dimensional (2D) materials^{2,3}, but fundamental challenges remain in achieving ultrahigh carrier concentration beyond the dielectric breakdown limit and in precisely defining local charge modulation with nanoscale spatial resolution⁴⁻⁸. Although alternative doping methods such as electrolyte gating and chemical intercalation9-12 are capable of inducing high carrier densities, they inevitably introduce disorder and unintentional electrochemical reactions that degrade device mobility^{13,14}. Additionally, these methods are not suitable for local charge modulation and realistic commercial device implementation. Other techniques, such as using lithographically defined gates⁴⁻⁸ or molecular self-assemblies on surfaces^{15,16}, can achieve impressive spatially controlled charge doping, but they cannot achieve simultaneous high carrier concentrations. They face additional limitations in applications that require rewritability or complex circuit designs.

Recent developments in van der Waals (vdW) heterostructures have led to alternative approaches to doping/gating that do not require complex processing masks or resists and with possible high mobility and high carrier concentration. For example, photo-induced doping and doping using voltage pulses from the tip of a scanning tunnelling microscope (STM) have been demonstrated^{17,18}. Both methods operate by activating defects within a hexagonal boron nitride (BN) layer¹⁹ that electrostatically influences the adjacent graphene layer. Although intriguing, these methods suffer from limited spatial resolution or cannot be scaled to mesoscopic lengths. Some attempts have also been made to achieve nand p-doping in graphene and other 2D materials via more flexible electron-beam irradiation using a scanning electron microscope (SEM)²⁰⁻²⁴. The focused electron beam also enables direct writing

of doping patterns into a single graphene layer^{20,22,23}. However, these efforts have faced common challenges including unstable doped states, inevitable degradation of device quality and limited controllability of doping concentrations^{20–24}.

In this Article, we report a fully reversible electron-beam-induced doping scheme for graphene and MoS_2 vdW heterostructures. We employ a BN-encapsulated device geometry, which protects the 2D materials from direct electron-beam irradiation²⁵ and enables non-volatile doping, which is further controlled by a back-gate electric field. With this approach, we can precisely tune the carrier density in the 2D materials in preselected spatially defined regions with nanoscale resolution. The doping regions persist even after the electron beam and back-gate voltage are removed, and are entirely rewritable. Importantly, we achieve high electron and hole carrier densities beyond $\pm 1 \times 10^{13}$ cm⁻² in a single back-gate BN/graphene/BN heterostructure device while maintaining ultrahigh room-temperature mobility at the theoretical phonon-scattering limit²⁶. We also realize similar doping effects in a MoS_2 device with decreased subthreshold swing (SS) compared with the device before doping.

Electron-beam-induced doping scheme and electrical measurements

The experimental scheme for the combined electron-beam/back-gate doping technique is illustrated in Fig. 1 (see Methods). Doping was performed in a standard SEM with electrical feedthroughs, which allow for in situ transport measurements. All graphene and MoS₂ devices were encapsulated by BN layers. This avoided the deposition of contaminants or electron-beam-induced reactions on the graphene or MoS₂ surface, which can introduce disorder and degrade mobility²⁵. The heterostructure was kept in vacuum at room temperature and the SEM-generated electron beam, with energy ranging from 1 keV to 30 keV, was used for exposure.

¹Department of Physics, University of California, Berkeley, CA, USA. ²Materials Sciences Division, Lawrence Berkeley National Laboratory, Berkeley, CA, USA. ³Kavli Energy NanoSciences Institute at the University of California and the Lawrence Berkeley National Laboratory, Berkeley, CA, USA. ⁴National Institute for Materials Science, Tsukuba, Japan. *e-mail: azettl@berkeley.edu

ARTICLES NATURE ELECTRONICS

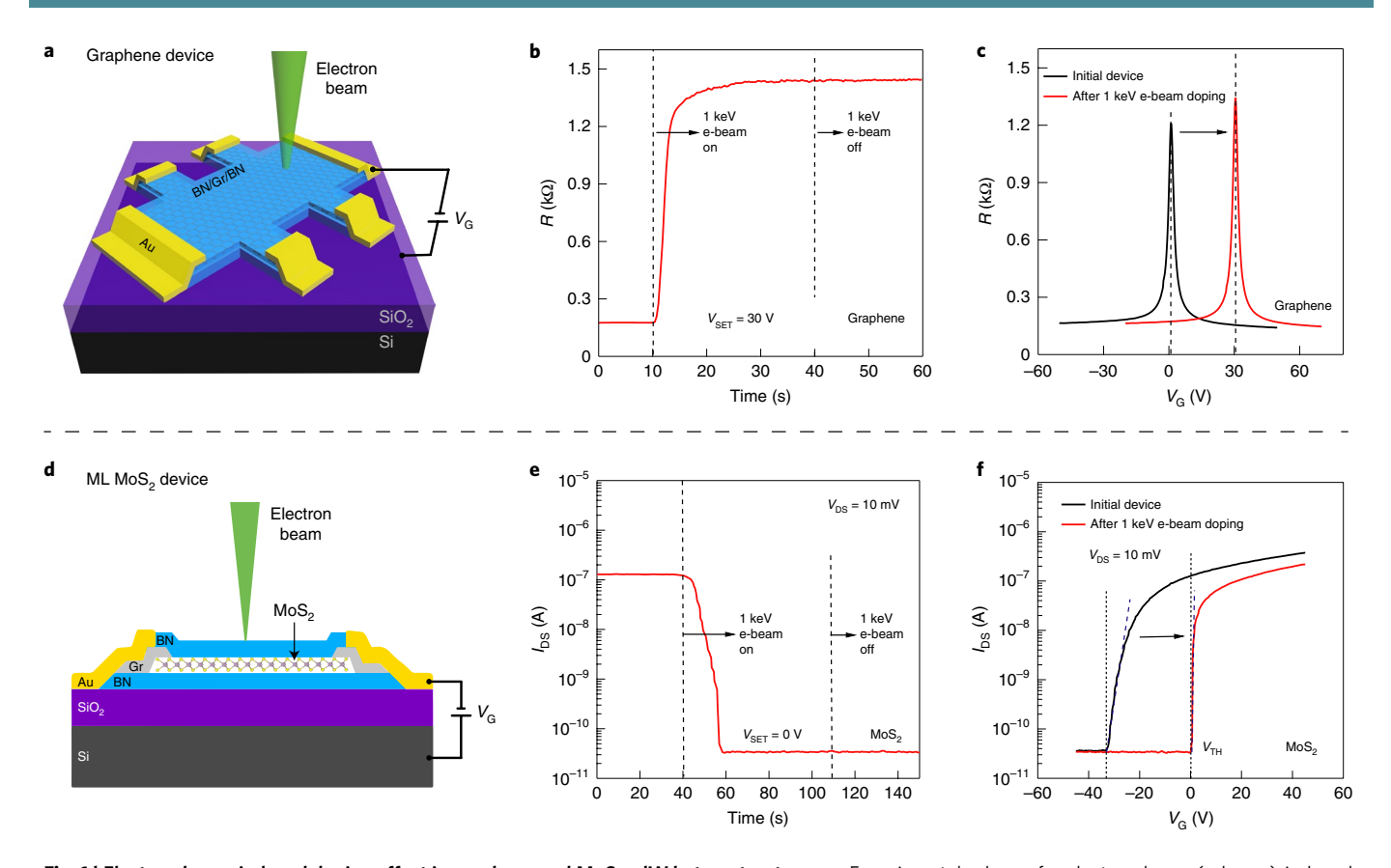


Fig. 1 [Electron-beam-induced doping effect in graphene and MoS₂ vdW heterostructures. a, Experimental scheme for electron-beam (e-beam)-induced doping in a graphene (Gr) device. Charge doping is induced in BN/Gr/BN by exposing it to a scanning electron beam (1-30 keV) in a standard SEM for a few seconds while holding the back-gate voltage $V_G \neq 0$ V. **b**, Resistance change of monolayer (ML) graphene (device 1) when a 1 keV electron beam is switched on and off (controlled by the beam blanker in the SEM) with V_G set to 30 V. $V_{DS} = 50 \,\mu\text{V}$ for the graphene measurements. **c**, Transfer curves $R(V_G)$ of the ML graphene before and after electron beam exposure. The CNP value is shifted from 0 V to 30 V (= V_{SET}), and the graphene has become uniformly hole-doped. **d**, Cross-sectional view of the experimental scheme for electron-beam doping in a BN-encapsulated ML MoS₂ transistor device with multilayer graphene contacts. **e**, Source-drain current I_{DS} change in ML MoS₂ when a 1 keV electron beam is switched on and off with V_G set to 0 V. **f**, $I_{DS}(V_G)$ of ML MoS₂ before and after electron beam exposure. The threshold voltage V_{TH} is shifted from −33 V to 0 V (= V_{SET}), and the calculated SS decreases more than one order of magnitude after doping (Supplementary Fig. 4).

Figure 1b,c illustrates the electron-beam-induced doping effect in graphene. The graphene device is initially undoped, and its charge neutral point (CNP), V_{CNP} is close to 0 V. With applied $V_G = 30 \text{ V}$, the device resistance R drops from $1.2 \text{ k}\Omega$ at the CNP to 180 Ω as the back-gate field moves the device off the CNP. At t = 10 s (Fig. 1b), the 1 keV SEM electron beam is turned on and scanned over the entire device (see Methods) while V_G is maintained at the preset voltage, $V_{\text{SET}} = 30 \text{ V}$. As Fig. 1b shows, within several seconds, R increases (Supplementary Note 5 and Supplementary Fig. 6) and saturates near $\sim 1.4 \, k\Omega$, close to the pre-doped CNP resistance of $1.2 \,\mathrm{k}\Omega$. At $t = 40 \,\mathrm{s}$, the electron beam is blanked, but R remains locked and high at $1.4 \text{ k}\Omega$; the device is now stably doped. As shown in Fig. 1c, the CNP has been shifted by 30 V after exposure, equal to the V_{SET} applied during the doping process. The same doping process is also applicable to MoS₂ transistor devices, as shown in Fig. 1d-f. The monolayer (ML) MoS₂ device is initially electron-doped with threshold voltage $V_{\rm TH} = -33$ V. After 1 keV electron-beam exposure at $V_{\text{SET}} = 0 \text{ V}$ (Fig. 1e), V_{TH} is shifted to 0 V (Fig. 1f). The graphene retains a very high field-effect mobility of ~5×104 cm² V⁻¹ s⁻¹, and the MoS₂ also retains a high mobility of ~130 cm² V⁻¹ s⁻¹ at room temperature. Notably, the graphene response curve after doping is even slightly sharper than the initial curve (Fig. 1c) and the SS of the MoS₂ device is one order of magnitude smaller after electron-beaminduced doping (Supplementary Note 3 and Supplementary Figs. 3

and 4), indicating an overall reduction of charge inhomogeneity in the devices.

Gate bias and energy dependence of electron-beaminduced doping

By employing different V_{SET} values during the doping process, preselected doping levels can be 'written' into the device. The process can be applied multiple times (with different V_{SET}) to the same device and is fully reversible. Figure 2a,b shows, respectively, the transport characteristics of the same graphene and MoS2 devices after successive doping with a 1 keV electron beam with different V_{SETP} respectively. The 1 keV electron-beam-induced doping causes a shift of the CNP (ΔV_{CNP}) or threshold voltage (ΔV_{TH}) close to the V_{SET} value both for electron and hole doping with the polarity controlled by V_{SET} . Remarkably, all transfer curves preserve the same sharp features, indicating little device degradation, even after multiple exposures with a 1 keV electron beam. This is in clear contrast to previous electron-beam-induced doping reports, which all showed inevitable mobility degradation²⁰⁻²⁴. Notably, our electron beam doping does not cause a 2H to 1T phase transition^{27,28} in MoS, (Supplementary Note 18 and Supplementary Fig. 27) due to the low dosage exposure and BN encapsulation, in contrast to previous reports²⁰.

The electron-beam doping process is sensitive to the electronbeam energy. Even for the same device, doping achieved using an NATURE ELECTRONICS ARTICLES

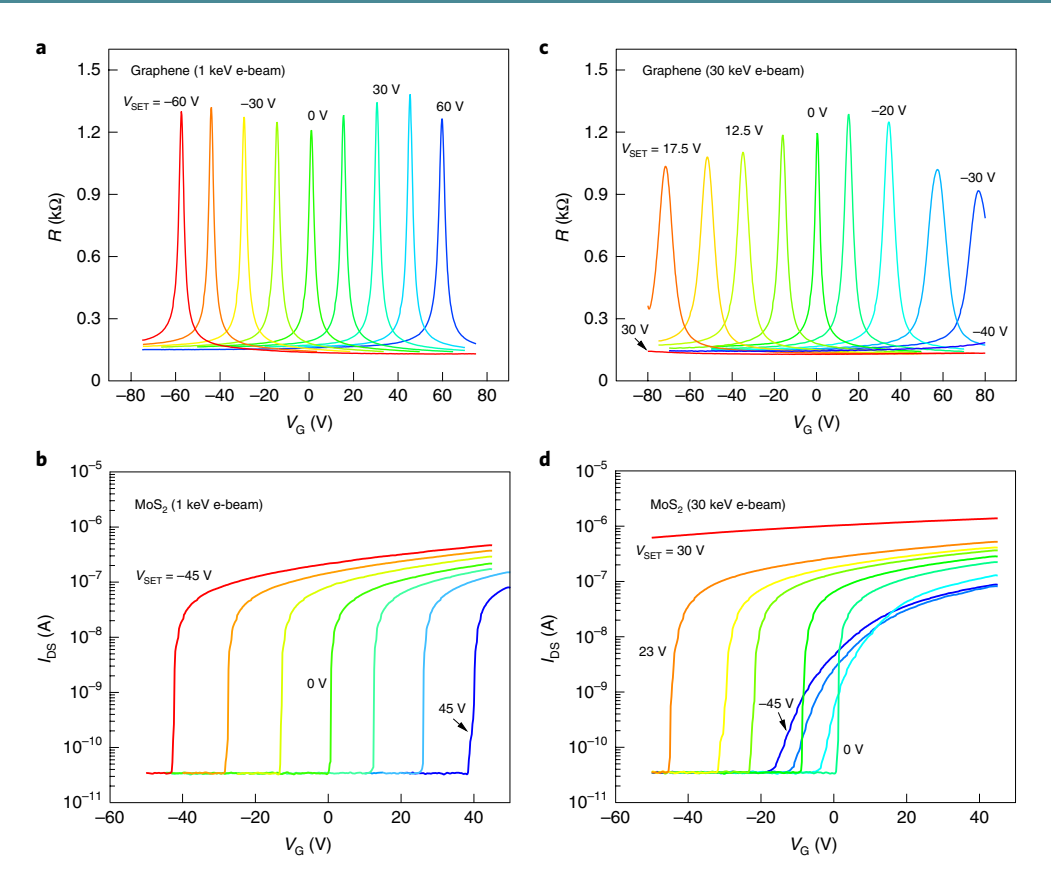


Fig. 2 | Energy dependence of electron-beam-induced doping effect in graphene and MoS₂ vdW heterostructures. **a**, Transfer curves $R(V_G)$ of graphene following successive electron-beam-induced doping using an electron-beam energy of 1 keV. $V_{SET} = -60$, -45, -30, -15, 0, 15, 30, 45 and 60 V, respectively (from red to blue). **b**, $I_{DS}(V_G)$ of ML MoS₂ after electron-beam exposure using an electron-beam energy of 1 keV. $V_{SET} = -45$, -30, -15, 0, 15, 30 and 45 V, respectively (from red to blue). $V_{DS} = 10$ mV for the MoS₂ measurements. **c**, Same as in **a**, but using a beam energy of 30 keV. $V_{SET} = 30$, 17.5, 15, 12.5, 10, 0, -10, -20, -25, -30 and -40 V, respectively (from red to blue). **d**, Same as in **b** but using a beam energy of 30 keV. $V_{SET} = 30$, 23, 22, 21, 20, 0, -15, -30 and -45 V, respectively (from red to blue).

electron-beam energy of 30 keV is qualitatively different than that obtained using an electron-beam energy of 1 keV, suggesting different mechanisms behind doping with a 1 keV beam versus a 30 keV beam. Figure 2c,d shows the transport properties of the same graphene and MoS2 devices after 30 keV electron-beam-induced doping with different V_{SET} . Hysteresis and leakage current measurements are presented in Supplementary Note 6 and Supplementary Figs. 13 and 14. Here, for a given V_{SET} we observe an opposite doping effect in Fig. 2c compared to the 1 keV case in Fig. 2a. When a positive V_{SFT} is applied, the graphene CNP shifts to a negative value, corresponding to n-doping (whereas a positive V_{SET} leads to p-doping in the 1 keV case). Moreover, the CNP is shifted to a much larger value than $|V_{\text{SET}}|$, indicating a higher doping concentration induced using a 30 keV electron-beam doping than for the 1 keV case. For 30 keV electron-beam doping, the field-effect mobility shows a slight doping dependence, but the sample still achieves a remarkably high room-temperature mobility, with $\mu_{\text{FET}} \approx 3 \times 10^4 \,\text{cm}^2 \,\text{V}^{-1} \,\text{s}^{-1}$ for a doping concentration of $\pm 5 \times 10^{12}$ cm⁻² (Supplementary Note 2 and Supplementary Fig. 2). The 30 keV electron-beam doping can induce highly doped states even beyond $\pm 1 \times 10^{13}$ cm⁻² with relatively small V_{SET} values. For example, as shown in Fig. 2c, the graphene device can be highly doped and the CNP moved far beyond $-80 \,\mathrm{V}$ for $V_{\mathrm{SET}} = 30 \,\mathrm{V}$. Figure 2d shows a similar doping effect in MoS₂ for the 30 keV electron-beam exposure. A highly electron-doped state is achieved for $V_{\text{SET}} = 30 \text{ V}$ (red curve, Fig. 2d), the opposite of what occurs in the 1 keV case (Fig. 2b). We also observed a reduction of the field-effect mobility for $V_{\text{SET}} = -45 \,\text{V}$,

which further indicates that high-energy electron-beam exposure causes doping in devices through a different mechanism than low-energy electron-beam exposure. We note that the electron-beam-induced doping effects are reproducible and repeatable in multiple devices and for multiple cycles (Supplementary Notes 1 and 7 and Supplementary Figs. 1 and 15). Moreover, the doped device is quite stable even in an ambient environment (Supplementary Note 5 and Supplementary Figs. 7–12).

Electrical characterization of highly doped devices

Next, we focus on the BN/Gr/BN heterostructure and characterize the device performance after electron-beam-induced doping. We employ Hall effect measurements to explicitly determine the doping concentrations and mobilities for both highly n- and p-doped states (Supplementary Note 4 and Supplementary Fig. 5). For 30 keV electron-beam doping, the doping concentration easily reaches $\sim 1.7 \times 10^{13} \,\mathrm{cm}^{-2}$ for n-doping and $\sim -1 \times 10^{13} \,\mathrm{cm}^{-2}$ for p-doping. Such high carrier concentrations cannot typically be achieved with conventional SiO₂ back-gated devices, as the required back-gate voltage would greatly exceed the breakdown voltage of the BN/SiO₂ dielectric. Figure 3a shows the Hall mobility μ_{Hall} as a function of carrier density n_{Hall} for both n- and p-doped devices induced by 30 keV electron-beam doping. The Hall mobility at 300 K is close to $10^4 \,\mathrm{cm^2 \, V^{-1} \, s^{-1}}$ for a doping concentration of $1.7 \times 10^{13} \,\mathrm{cm^{-2}}$, comparable to the acoustic-phonon-limited mobility predicted for intrinsic graphene^{26,29,30} (Supplementary Note 10). The room-temperature mobility reported here in the high-carrier-density regime beyond ARTICLES NATURE ELECTRONICS

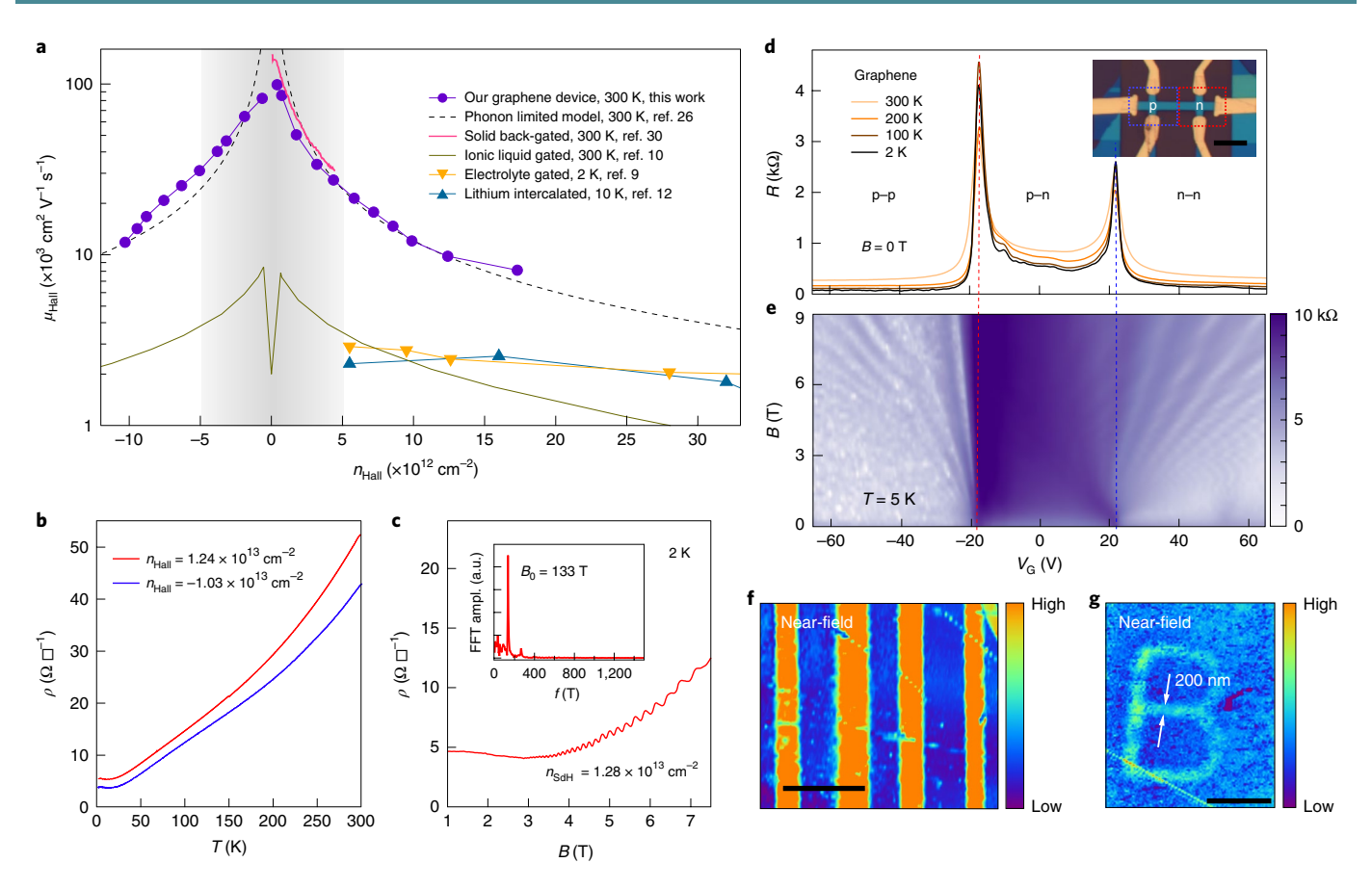


Fig. 3 | Transport characteristics and spatially controlled nanoscale doping patterns of BN/Gr/BN heterostructures by electron-beam-induced doping. **a**, Hall effect mobility versus carrier density for 30 keV electron-beam-doped ML graphene samples at 300 K compared to other highly doped ML graphene samples reported in the literature. The grey shaded region indicates the conventional back-gate accessible carrier density regime. **b**, Four-terminal sheet resistivity ρ of 30 keV electron beam highly electron- and hole-doped ML graphene devices, showing metallic behaviour. **c**, Resistivity ρ of the electron-doped device in **b** measured as a function of magnetic field B at 2 K, showing well-defined periodic SdH oscillations. The corresponding carrier density $n_{\rm SdH}$ is 1.28×10^{13} cm⁻², derived from the peak position of the Fourier transform as shown in the inset. **d**, Generation of a p-n junction in a BN/Gr/BN heterostructure by controlled electron-beam exposure in lithography mode. The temperature dependence of four-terminal resistance R versus $V_{\rm G}$ was measured after writing the p-n junction at 300 K. Inset: the device geometry. Scale bar, 5 μm. **e**, Log-scale plot of longitudinal four-terminal resistance R of the graphene p-n junction as a function of magnetic field and gate voltage at 5 K. **f**, **g**, s-SNOM images of a stripe pattern and a letter 'B' pattern written in a BN/Gr/BN heterostructure using a 2 keV electron beam at $V_{\rm SFT} = 55$ V. Scale bars, 2 μm (**f**) and 1 μm (**g**). The spatial resolution is ~200 nm, as indicated by the arrows in **g**.

 $\pm 5 \times 10^{12}$ cm⁻² (outside the shaded region in Fig. 3a) is much higher than in other reports, even five times higher than the mobility accessed by ionic liquid gating¹⁰, electrolyte gating⁹ and lithium intercalation¹² on monolayer graphene devices (Fig. 3a).

In the high-carrier-density regime, the four-terminal sheet resistivity ρ for our devices is ~40 Ω \Box ^{-1} (Fig. 3b) at 300 K, comparable to the record sheet resistivity for graphene^{9,30}. As shown in Fig. 3b, ρ decreases monotonically with temperature for both electron- and hole-doped devices, showing metallic behaviour. It follows a linear T dependence in the high-temperature regime (30 K < T < 160 K) and saturates to a very low residual resistance in the low-temperature limit^{9,12,30}. This reflects the cleanness of our device, even in the high-density regime. Figure 3c shows well-defined Shubnikov-de Haas (SdH) oscillations in the same electron-doped device at a temperature of 2 K with a carrier density $n_{\rm SdH}$ of $1.28 \times 10^{13} \, {\rm cm}^{-2}$, consistent with $n_{\rm Hall}$. The Hall effect mobility at 2 K reaches $1 \times 10^5 \, {\rm cm}^2 \, {\rm V}^{-1} \, {\rm s}^{-1}$. This reflects a homogeneous, high-density, ultrahigh-mobility two-dimensional electron gas in our device.

Direct electron-beam writing of nanoscale doping patterns

The electron-beam activation process enables the writing of spatially complex doping patterns with high resolution in a single vdW

heterostructure device, without the need for complex gating electrodes, ionic fluids or the deposition of foreign chemical species. By using the lithography function in the SEM, the electron beam can be positioned to different target regions and thus be used to draw arbitrary patterns with nanoscale precision. Here we demonstrate the creation of a high-quality graphene p-n junction by electron-beaminduced doping. As shown in the inset of Fig. 3d, we use the lithography mode of the SEM to selectively expose the region enclosed by the red rectangle and the blue rectangle to a 2keV electron beam while holding V_{SET} to approximately $-20\,\text{V}$ and $20\,\text{V}$, respectively. These two regions thus respectively become electron- and holedoped. Two distinct sharp peaks are observed when measuring electrical resistance across the whole device, showing a separation of the CNP of ~40 V. This is the clear characteristic feature of a high-quality graphene p-n junction, vastly superior to those obtained in previous reports^{15,17,23}. The p-n junction was further investigated at low temperature. While in the quantum Hall regime, there are three distinct regions that can be tuned with the global back-gate: p-p, p-n and n-n. Figure 3e shows the longitudinal resistance across the p-n junction while varying the magnetic field and the carrier density. In the p-n junction region, the longitudinal resistance jumps into an insulating state due to the quantum Hall edge states counterpropagating NATURE ELECTRONICS ARTICLES

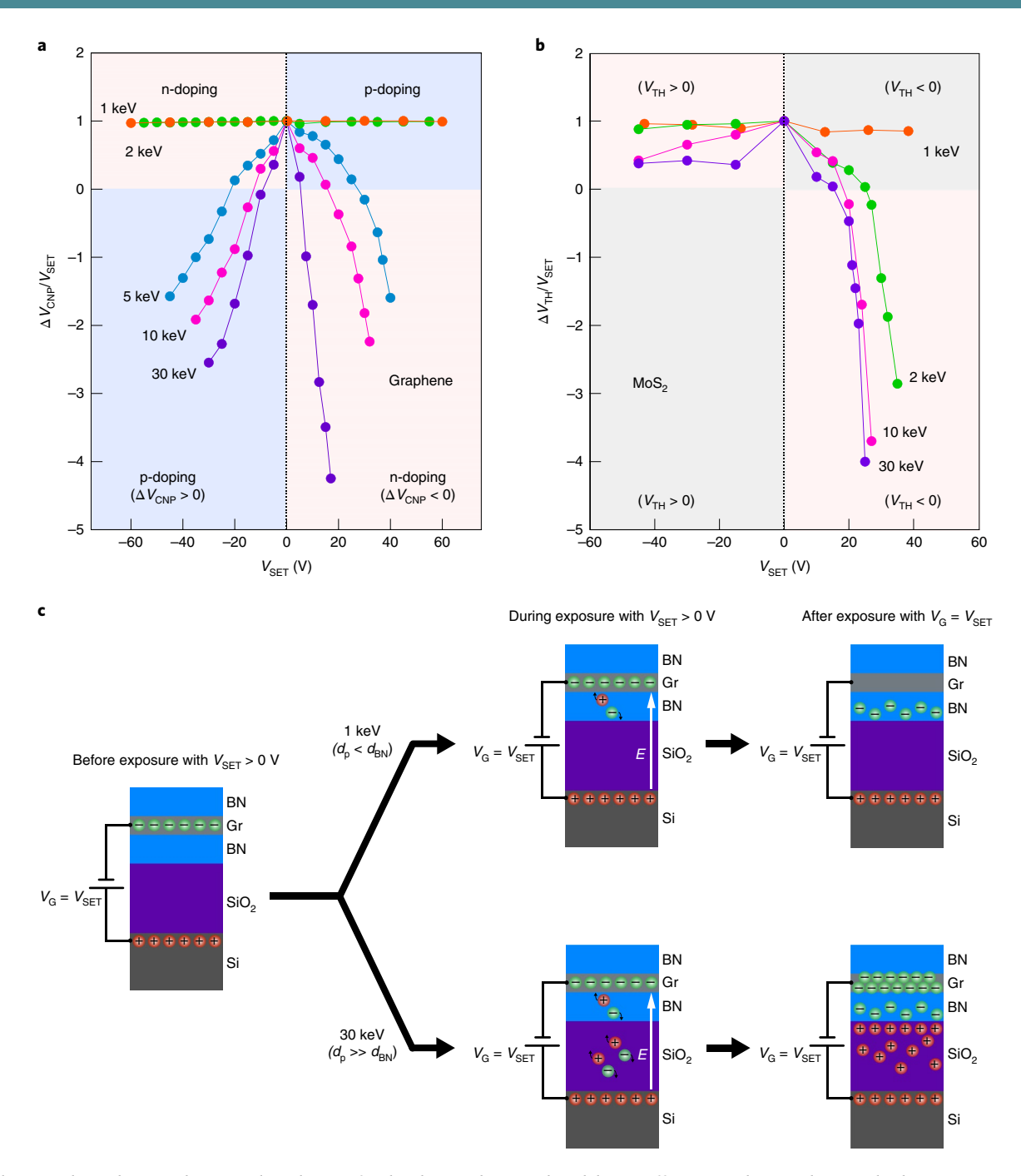


Fig. 4 | Energy dependence and proposed mechanism for the electron-beam-induced doping effect in graphene and MoS_2 vdW heterostructures. **a**, Normalized effective capacitance defined as $\Delta V_{CNP}/V_{SET}$ versus the corresponding V_{SET} for the electron-beam doping effect in graphene at different electron-beam energies. Red and blue shaded regions indicate electron and hole doping induced by electron-beam exposure, respectively. **b**. Normalized

electron-beam energies. Red and blue shaded regions indicate electron and hole doping induced by electron-beam exposure, respectively. **b**, Normalized effective capacitance defined as $\Delta V_{\text{TH}}/V_{\text{SET}}$ versus V_{SET} for the electron-beam doping effect in ML MoS₂ at different electron-beam energies. **c**, Schematic of the doping process and charge carrier distribution for 1keV and 30 keV electron-beam doping in BN/Gr/BN at positive V_{SET} . Here, d_p is the penetration depth of the electron beam and d_{BN} is the total BN thickness. In both scenarios, the device is kept at $V_{\text{G}} = V_{\text{SET}}$ after electron-beam exposure. A more detailed schematic of the doping process is provided in Supplementary Figs. 22 and 23.

and interfering with each other^{4,15}. Meanwhile, in the p–p region and n–n region, there are edge states that propagate in the same direction and mix in the channel, as manifested in the Landau fan diagram. This proves that our technique preserves the high mobility of the device after patterning and can be used to engineer quantum states. Moreover, it is highly reconfigurable and a p–i–n junction is also created after erasing the previously written p–n junction in the same device (Supplementary Note 7 and Supplementary Fig. 16).

The lithography mode of the SEM allows the writing of more sophisticated doping patterns at high spatial resolution down to 200 nm. We used scattering-type scanning near-field optical microscopy (s-SNOM) and electrostatic force microscopy (EFM) to image some of the patterns we created (see Methods). Figure 3f,g shows s-SNOM images of a stripe pattern and a letter 'B' pattern drawn using the electron-beam lithography mode with $V_{\rm SET} = 55 \, {\rm V}$ and a beam energy of 2 keV (for the dosage parameters

ARTICLES NATURE ELECTRONICS

see Supplementary Note 8). The s-SNOM image clearly reveals a striped doping modulation (Supplementary Note 8 and Supplementary Fig. 17) resulting from the different scattering amplitudes of the infrared light in response to different local carrier densities. The letter 'B' pattern has a line width of ~200 nm, a significant improvement over previous results^{17,19}. This spatial resolution is confirmed with our EFM measurement (Supplementary Note 9 and Supplementary Fig. 18). We remark that our intrinsic doping line width may be even smaller, because our EFM analysis neglects line charge electric-field divergence.

Proposed doping mechanism

We now turn to the electron-beam energy-dependent doping mechanism. It is revealing to plot the normalized effective capacitance $\Delta V_{\rm CNP}/V_{\rm SET}$ and $\Delta V_{\rm TH}/V_{\rm SET}$ versus $V_{\rm SET}$ (proportional to the electric field) for the graphene and MoS2 devices, as shown in Fig. 4a,b, respectively. For low-beam-energy (1 keV) exposures, $\Delta V_{\rm CNP}/V_{\rm SET}$ and $\Delta V_{\text{TH}}/V_{\text{SET}}$ remain nearly constant at unity, independent of V_{SET} . For higher-beam-energy (\gg 1 keV) exposures, $\Delta V_{\text{CNP}}/V_{\text{SET}}$ and $\Delta V_{\mathrm{TH}}/V_{\mathrm{SET}}$ are strongly dependent on V_{SET} and the electron-beam energy. Doping with a 30 keV exposure results in an effective capacitance more than four times higher than the dielectric capacitance for electron doping. This indicates an electric-field- and irradiationboosted charge accumulation process. MoS, exhibits an asymmetric behaviour and here it is more difficult to access hole conduction compared to graphene, possibly because MoS2 has a large bandgap and the device is intrinsically electron-doped. Nevertheless, the similar energy- and electric-field dependence of the doping effects suggests a general doping mechanism for our electron-beam doping process in vdW heterostructures.

Here, we propose a preliminary model for the doping mechanism, but a full quantitative understanding requires further experimental and theoretical study. During electron-beam exposure of the vdW heterostructures, there are a variety of processes occurring (secondary electron emission, plasmon decay and so on)³¹, but the primary effects that contribute to the doping are electron-hole pair generation and trap states in the dielectrics³² Taking graphene as an example, for low electron-beam energy (1 keV and 2 keV), the electron beam primarily excites electron-hole pairs in the bottom BN layers (Supplementary Note 12 and Supplementary Fig. 20); that is, the electron-beam penetration depth d_p is smaller than the BN thickness d_{BN} (Fig. 4c). For the case of $V_{SET} > 0$, hot electrons drift towards the silicon due to the gate electric field E applied by V_{SET} but are trapped in BN defects near the BN/SiO₂ interface. When there is enough charge in the BN trap states to screen the gate electric field, the charging process stops and the graphene becomes charge neutral at V_{SET} after electron-beam exposure, as shown in Fig. 4c (top).

For high-energy electron-beam exposure (30 keV), electronhole pairs are generated in both the bottom BN and SiO₂ ($d_p \gg d_{BN}$; also see Supplementary Fig. 20), whereupon they separate due to the electric field E. With $V_{\text{SET}} > 0$, electron traps are activated in the BN near the BN/SiO₂ interface, while hole traps are activated in the SiO₂ near the BN/SiO₂ interface. These charge traps reduce the potential drop, but the total applied potential drop must equal V_{SET} so more charge is accumulated in the dielectrics until an equilibrium distribution is reached. Given that the SiO₂ layer is much thicker and has a higher defect density than the BN layer¹⁹, more holes are trapped in SiO₂ than electrons in BN, as shown in Fig. 4c. Consequently, the combined doping effects of activated defects is opposite for a high-energy (30 keV) versus a low-energy (1 keV) electron beam. More control experiments and a detailed discussion of the proposed mechanism are provided in Supplementary Notes 11-14 and Supplementary Figs. 19-23. This model can also be applied to MoS₂ to account for the similar energy-dependent reversed doping effects, but admittedly further development of the model is required

to explain all the subtleties of the doping behaviour, such as asymmetries in p- and n-type doping behaviour.

Conclusions

We have reported an electron-beam-induced doping technique for BN-encapsulated vdW heterostructures. The technique provides a reversible method to write complex and non-volatile doping patterns with high spatial resolution, high carrier density and high mobility, even at room temperature. We demonstrate this by directly writing p–n junctions and nanoscale patterns, as well as achieving electron and hole carrier densities beyond $\pm 1\times 10^{13}\,\mathrm{cm^{-2}}$ with high mobility in a BN/graphene/BN heterostructure device. We also show similar controlled doping in MoS $_2$ devices. Our method provides a route to create multi-component nanoscale circuitry in vdW heterostructures with minimal processing. It may also be an ideal approach to pattern superlattice potentials or customize the electronic properties of 2D materials for novel scientific studies and device applications.

Methods

Device fabrication. High-quality BN crystals from Taniguchi and Watanabe were exfoliated onto $285\,\mathrm{nm}$ SiO₂/Si substrates. We used BN flakes ranging in thickness from 8 to $40\,\mathrm{nm}$ for the top and bottom encapsulating layers. The BN-encapsulated graphene and MoS_2 vdW heterostructures were fabricated using the dry pick-up transfer technique³⁰ and then annealed in an Ar/H₂ forming gas for 3 h at 350 °C. The top BN layer is mandatory for high-mobility devices as it prevents environmental surface contamination from reaching the critical graphene layer (Supplementary Note 15 and Supplementary Fig. 24). Standard electron-beam lithography processes were used to pattern etching masks and electrodes onto the heterostructures. The thickness information for all the devices is provided in Supplementary Note 17, Supplementary Table 1 and Supplementary Fig. 25.

Electron-beam doping process. The heterostructure device was mounted in a SEM (model, FEI XL30 Sirion) using a custom holder attached to an electrical feedthrough for doping and limited in situ transport measurement (Supplementary Note 17 and Supplementary Fig. 26). We used a standard a.c. voltage bias lock-in technique at 97.13 Hz to measure the transport properties of the device in the SEM chamber under a vacuum of 3×10^{-6} mbar at room temperature. Electron-beam energies ranging from $1\,\mathrm{keV}$ to $30\,\mathrm{keV}$ with beam current I_c ranging from $1\,\mathrm{pA}$ to $15\,\mathrm{pA}$ were used for the electron-beam-induced doping.

Both normal scanning mode and lithography mode were implemented to study the doping effect and write pre-designed doping patterns on the BN-encapsulated graphene and MoS_2 devices. For electron-beam irradiation in the normal scanning mode, the exposed area S was $\sim 300~\mu\text{m}^2$, including the whole heterostructure region. Resistance was monitored during exposure and the exposure stopped when the irradiation-induced resistance change had stabilized. The typical exposure time t ranged from 30 to 120 s. The accumulated irradiation dosage D is given by $D = I_c t/Se$. For example, for I = 10~pA, $S = 300~\mu\text{m}^2$ and t = 60~s, $D = 200~\mu\text{C}~\text{cm}^{-2}$ (that is, $12.5~\text{e}^-$ nm $^{-2}$). Once the resistance had stabilized under a certain preset voltage V_{SET} during irradiation, additional exposure did not cause further resistance changes. For the lithography mode, we tested different dosage parameters. To achieve high spatial resolution, a smaller dosage parameter was beneficial (Supplementary Notes 8 and 9 and Supplementary Figs. 17 and 18).

Low-temperature transport measurements were performed in a Quantum Design PPMS system after quickly transferring the doped sample from the SEM without significant exposure to ambient light (Supplementary Note 5 and Supplementary Fig. 12).

Near-field nano-imaging. We used s-SNOM to obtain near-field images of the samples. The s-SNOM is based on a tapping-mode AFM. An infrared light beam $(\lambda\!=\!10.6\,\mu\text{m})$ was focused onto the apex of a conductive AFM tip, then an MCT detector placed in the far field was used to collect the scattered light, which carries the local optical information of the sample. Near-field images were recorded simultaneously with the topographic information during the measurements. The optical contrast of doped and undoped areas in the near-field images stems from the different local carrier densities, which result in different scattering amplitudes of the infrared light.

Data availability

The data that support the plots within this paper and other findings of this study are available from the corresponding author upon reasonable request.

Received: 20 March 2019; Accepted: 4 December 2019; Published online: 20 January 2020

NATURE ELECTRONICS ARTICLES

References

- 1. Hu, C. Modern Semiconductor Devices for Integrated Circuits (Pearson, 2010).
- 2. Novoselov, K. S. et al. Electric field effect in atomically thin carbon films. *Science* **306**, 666–669 (2004).
- Lui, C. H., Li, Z., Mak, K. F., Cappelluti, E. & Heinz, T. F. Observation of an electrically tunable band gap in trilayer graphene. *Nat. Phys.* 7, 944–947 (2011).
- Williams, J. R., DiCarlo, L. & Marcus, C. M. Quantum Hall effect in a graphene p-n junction. Science 317, 638-641 (2007).
- Özyilmaz, B. et al. Electronic transport and quantum Hall effect in bipolar graphene p-n-p junctions. *Phys. Rev. Lett.* 99, 2-5 (2007).
- Huard, B. et al. Transport measurements across a tunable potential barrier in graphene. Phys. Rev. Lett. 98, 8–11 (2007).
- 7. Liu, G., Velasco, J., Bao, W. & Lau, C. N. Fabrication of graphene p-n-p junctions with contactless top gates. *Appl. Phys. Lett.* **92**, 1–4 (2008).
- Dubey, S. et al. Tunable superlattice in graphene to control the number of Dirac points. *Nano Lett.* 13, 3990–3995 (2013).
- Efetov, D. K. & Kim, P. Controlling electron-phonon interactions in graphene at ultrahigh carrier densities. *Phys. Rev. Lett.* 105, 2–5 (2010).
- Ye, J. et al. Accessing the transport properties of graphene and its multilayers at high carrier density. Proc. Natl Acad. Sci. USA 108, 13002–13006 (2011).
- 11. Shi, W. et al. Superconductivity series in transition metal dichalcogenides by ionic gating. Sci. Rep. 5, 12534 (2015).
- Zhao, S. Y. F. et al. Controlled electrochemical intercalation of graphene/h-BN van der Waals heterostructures. Nano Lett. 18, 460–466 (2018).
- Xia, Y., Xie, W., Ruden, P. P. & Frisbie, C. D. Carrier localization on surfaces of organic semiconductors gated with electrolytes. *Phys. Rev. Lett.* 105, 36802 (2010).
- Ovchinnikov, D. et al. Disorder engineering and conductivity dome in ReS₂ with electrolyte gating. Nat. Commun. 7, 12391 (2016).
- Lohmann, T., Von Klitzing, K. & Smet, J. H. Four-terminal magnetotransport in graphene p-n junctions created by spatially selective doping. *Nano Lett.* 9, 1973–1979 (2009).
- Ojeda-Aristizabal, C. et al. Molecular arrangement and charge transfer in C₆₀/graphene heterostructures. ACS Nano 11, 4686–4693 (2017).
- Ju, L. et al. Photoinduced doping in heterostructures of graphene and boron nitride. Nat. Nanotechnol. 9, 348–352 (2014).
- Velasco, J. et al. Nanoscale control of rewriteable doping patterns in pristine graphene/boron nitride heterostructures. *Nano Lett.* 16, 1620–1625 (2016).
- Wong, D. et al. Characterization and manipulation of individual defects in insulating hexagonal boron nitride using scanning tunnelling microscopy. *Nat. Nanotechnol.* 10, 949–953 (2015).
- 20. Zhou, Y. et al. Programmable graphene doping via electron beam irradiation. *Nanoscale* **9**, 8657–8664 (2017).
- Childres, I. et al. Effect of electron-beam irradiation on graphene field effect devices. *Appl. Phys. Lett.* 97, 173109 (2010).
- 22. Yu, X., Shen, Y., Liu, T., Wu, T. & Jie Wang, Q. Photocurrent generation in lateral graphene p–n junction created by electron-beam irradiation. *Sci. Rep.* 5, 12014 (2015).
- Iqbal, M. Z., Anwar, N., Siddique, S., Iqbal, M. W. & Hussain, T. Formation of p-n-junction with stable n-doping in graphene field effect transistors using e-beam irradiation. *Opt. Mater.* 69, 254–258 (2017).

- Stará, V., Procházka, P., Mareček, D., Šikola, T. & Čechal, J. Ambipolar remote graphene doping by low-energy electron beam irradiation. *Nanoscale* 10, 17520–17524 (2018).
- Teweldebrhan, D. & Balandin, A. A. Modification of graphene properties due to electron-beam irradiation. Appl. Phys. Lett. 94, 92–95 (2009).
- Hwang, E. H. & Sarma, S. Das Acoustic phonon scattering limited carrier mobility in two-dimensional extrinsic graphene. Phys. Rev. Lett. 77, 1–6 (2008).
- Katagiri, Y. et al. Gate-tunable atomically thin lateral MoS₂ Schottky junction patterned by electron beam. Nano Lett. 16, 3788–3794 (2016).
- 28. Xie, X. et al. Designing artificial 2D crystals with site and size controlled quantum dots. *Sci. Rep.* 7, 9965 (2017).
- Sule, N. & Knezevic, I. Phonon-limited electron mobility in graphene calculated using tight-binding Bloch waves. J. Appl. Phys. 112, 053702 (2012).
- Wang, L. et al. One-dimensional electrical contact to a two-dimensional material. Science 342, 614–617 (2013).
- Ausman, G. A. & McLean, F. B. Electron-hole pair creation energy in SiO₂. Appl. Phys. Lett. 26, 173–175 (1975).
- Curtis, O. L., Srour, J. R. & Chiu, K. Y. Hole and electron transport in SiO₂ films. *J. Appl. Phys.* 45, 4506–4513 (1974).

Acknowledgements

We thank Y. Chen, W. Ruan, S. Zhao, and J. Jung for useful discussions. This work was supported in part by the Director, Office of Science, Office of Basic Energy Sciences, Materials Sciences and Engineering Division, and Molecular Foundry of the US Department of Energy under contract no. DE-AC02-05-CH11231, primarily within the van der Waals Heterostructures Program (KCWF16), which provided for development of the concept and device fabrication, electron-beam doping and transport characterization, and within the sp2-Bonded Materials Program (KC2207), which provided for s-SNOM measurements, and by the National Science Foundation, under grant no.1542741, which provided for AFM topography and SdH measurements, and under grant no.1807233, which provided for EFM measurements.

Author contributions

A.Z., M.C., W.S., S.K., H.-Z.T. and D.W. conceived the experiment. S.K., W.S. and S.-Y.W. contributed to device fabrication. W.S. and S.K. performed all electrical measurements, EFM measurements and data analysis. K.W. and T.T. provided the BN crystals. L.J. and F.W. contributed to the s-SNOM measurements. W.S., S.K. and A.Z. co-wrote the manuscript, with inputs and comments from all authors.

Competing interests

The authors declare no competing interests.

Additional information

Supplementary information is available for this paper at https://doi.org/10.1038/s41928-019-0351-x.

Correspondence and requests for materials should be addressed to A.Z.

Reprints and permissions information is available at www.nature.com/reprints.

Publisher's note Springer Nature remains neutral with regard to jurisdictional claims in published maps and institutional affiliations.

© The Author(s), under exclusive licence to Springer Nature Limited 2020